WILEY-VCH

Rectification of mobile Leidenfrost droplets by planar ratchets

Jing Li[#], Xiaofeng Zhou[#], Yujie Zhang, Chonglei Hao, Fuwang Zhao, Minfei Li, Hui Tang, Wenjing Ye, and Zuankai Wang*

Dr. J. Li, Dr. C. Hao, M. Li, Prof. Z. Wang
Department of Mechanical Engineering, City University of Hong Kong, 999077, China

Dr. X. Zhou
Department of Electronic Engineering, East China Normal University, Shanghai 200241, China

Dr. Y. Zhang, Prof. W. Ye
Department of Mechanical and Aerospace Engineering, The Hong Kong University of Science and Technology, Hong Kong 999077, China

F. Zhao, Prof. H. Tang
Department of Mechanical Engineering, The Hong Kong Polytechnic University, Hong Kong 999077, China

Prof. Z. Wang
Shenzhen Research Institute of City University of Hong Kong, Shenzhen 518057, China

E-mail: zuanwang@cityu.edu.hk

Keywords: rectification, individual effect, collective coordination, Leidenfrost droplet, fluidic devices

Abstract

The self-transportation of mobile Leidenfrost droplets with well-defined direction and velocity on millimetric ratchets is one of the most representative and spectacular phenomena in droplet dynamics. Despite extensive progress in our ability to control the spatiotemporal propagation of droplets, it remains elusive how the individual ratchet units as well as the interactions within their arrays are translated into the collective droplet dynamics. Here we design simple planar ratchets characterized by uniform height normal to the surface. We reveal that on planar ratchets, the transport dynamics of Leidenfrost droplets is not only dependent on individual units, but also the elegant coordination within their arrays dictated by their topography. The design of planar ratchets enriches our fundamental understanding of how the surface topography is

translated into dynamic and collective droplet transport behaviors, and also imparts higher applicability in microelectromechanical system (MEMS) based fluidic devices.

Rectification of droplet transport at high temperature is of fundamental interest and practical importance [1]. Of special interest is the case where the imposed temperature is higher than the so-called Leidenfrost point [2, 3]. In this unique thermal state, droplets levitate above the substrate by a uniform vapor layer, and the conventional triple-phase interface is transformed into separate liquid/vapor and vapor/solid interfaces [4-8]. As a result, droplets stay in a thermodynamically quasi-stable state with elongated lifetime [9, 10] and enhanced mobility [11-13], providing extensive potentials in fluidic devices, energy conversion and drag reduction [11, 14-17]. Distinct from ambient or condensation condition where the droplets are usually manipulated by wetting gradient [18, 19] and topographical asymmetry [20-24], droplets at Leidenfrost state exhibit a self-activation and self-rotation without the need of any asymmetric features [25, 26].

The random self-propulsion of Leidenfrost droplets on the flat surface can be transformed into a preferential motion by the careful introduction of asymmetric structures [27-30]. Among them, the most widely-studied device is ratchets with slopes descending in the vertical direction. Despite the diversity in the length scales of these ratchets [31] or the types of droplets studied [15, 27, 32, 33], the evaporating vapor escapes both along and normal to the descending slopes, displaying a three-dimensional flow signature though the ratchets are spatially arranged in one-dimensional lattices [34, 35]. In this scenario, the requirement of ratchets with height gradient to allow the self-transportation of droplets also restricts their broad application in MEMS-based fluidic devices, which are normally based on thin silicon or glass substrates. More importantly, it remains unclear how the collective transport dynamics of vapor/droplet is affected or coordinated by these individual ratchets.

Here we are interested in whether the Leidenfrost droplets can be manipulated by two-dimensional (2D) geometry with the uniform height normal to the surface. More importantly, we focus on how these individual features and their group behaviors determine the general displays of droplet motions. Inspired by the 1D herringbone structure [28], we design surfaces consisting of asymmetric planar ratchets patterned in 2D lattices. Therefore, the individual planar ratchet serves as the first-order unit, whereas the interplay between these individual units arranged in lattices leads to the second-order asymmetry and collective function. We show that on planar ratchets, the evaporating vapor underneath the droplets escapes on a 2D plane, and its rectification ratio relies on the coordination of both the first-order ratchet units and second-order lattices. As a result, Leidenfrost droplets demonstrate different transport regimes with varying velocities and directions. In the followings, we explore the fundamental mechanisms and elucidate how the two-tier asymmetries of planar ratchets are translated to the controllable tunability in droplet dynamics.

Planar ratchets patterned in two-dimensional rectangular lattices were fabricated on silicon wafer by standard photolithography and deep reactive-ion etching. As shown in the scanning electron microscopy (SEM) image in Figure 1a, the slope of planar ratchets, or the first-order units, descends along $+X$ direction. The base length (D), the apex angle (θ), and the height (h) of planar ratchets are fixed at 100 µm, 37°, and 100 µm, respectively. In contrast, the spacings between these first-order units along X (L_X) and Y (L_Y) axes, or the length and width of lattices, vary ($L_X = 300$ µm and $L_Y = 150$ µm), giving rise to the cooperative second-order asymmetry. After heating the as-fabricated planar ratchets to the Leidenfrost point ($T_L = 300 \pm 6.0$ °C), the gently deposited droplet (radius $R_o = 1.31$ mm) is rectified into a preferential direction along the descending slope (or $+X$) (Figure 1b and Supporting Movie 1). Counterintuitively, without changing the geometry of individual ratchet, we found that a simple variation in second-order arrangement can lead to the pronounced response of droplet motions. As evidenced by Figures 1c and 1d, on surface with reverse second-order arrangements ($L_X = 150$ µm and $L_Y = 300$ µm;

$T_L = 305 \pm 6.1$ °C), the Leidenfrost droplet demonstrates a long-range transport against the descending slope (or -*X*; Supporting Movie 2). The rectification of Leidenfrost droplets by planar ratchets is in striking contrast to control surfaces consisting of symmetric rhombic first-order units patterned in asymmetric second-order lattices, where no any directional motion was observed regardless of the variation in L_X or L_Y (Figure S1 and Supporting Movie 3).

Figures 2a and b plot the time-dependent evolution of droplet velocities on planar ratchets with various second-order arrangements. In both cases, Leidenfrost droplets accelerate upon touching the substrates, eventually reaching a steady velocity. On the basis of the velocity curve, the real-time velocity is fitted as: $v(t) = -v_s e^{-\beta t/m} - v_s$, where β is the interfacial friction coefficient [27], v_s represents the steady velocity and m is the droplet mass. Accordingly, the acceleration (*a*) of droplet is calculated as $a = v_s \beta / m$. As a result, planar ratchets with $L_X = 300$ μm and $L_Y = 150$ μm yield an acceleration and steady velocity of 3.15 m/s^2 and 10.8 cm/s, respectively, in the +*X* direction, whereas ratchets with $L_X = 150$ μm and $L_Y = 300$ μm lead to an acceleration and steady velocity of -2.76 m/s^2 and -6.91 cm/s, respectively, following the -*X* direction. Notably, the droplet steady velocity manifested on different planar ratchets at Leidenfrost points are both comparable to that on traditional ratchets [27, 31, 32].

The self-propulsion of Leidenfrost droplet on planar ratchets is also sensitive to superheat (*T* - T_{sat}). Here *T* is the temperature at the back of substrate and T_{sat} represents the boiling point of water. As shown in Figure S2, the Leidenfrost droplets achieve high transport velocities at lower superheat. As the imposed temperature further increases from the Leidenfrost points, the steady velocities of Leidenfrost droplets on planar ratchets gradually decrease, and finally stabilized at 1.8 cm/s and -1.7 cm/s, respectively. Such a reduction in transport velocities can be explained by the growing vapor thickness as temperature increases, which screens the asymmetric structure as it gets thick enough (Figure S2b). To exclude shielding effect of thick vapor on the structural functionality and considering that the Leidenfrost points of planar

ratchets involved in this study fluctuate in a small range, in the followings, we mainly focused on the maximum steady velocity, or in other words, the steady velocity measured at Leidenfrost points.

To gain more detailed insights into the droplet transport dynamics, we compared the flow fields inside Leidenfrost droplets using Particle Image Velocimetry (PIV) (Figure S4 and Supporting Text) [36]. Regardless of different velocities and directions on various planar ratchets, Leidenfrost droplets always present the asymmetric and preferential rotating circulation cell, following the directions of their propagation (Figures 2d and 2e). Moreover, the occurrence of the maximum velocity field at the liquid/vapor interface with opposite direction strongly suggests that the different droplet transport direction arise from the varying viscous shear induced by the asymmetric vapor flow [25].

How does the occurrence of the two-tier asymmetries on planar ratchets mediates the vapor flow and the droplet transport dynamics? We start from the effect of second-order topography (L_X and L_Y) on the movement of Leidenfrost droplets under the same first-order topography. Here, the apex angle θ and base length D of first order unit are kept constant at 37° and 100 μm, respectively. Figure 3A presents the selected snapshots of Leidenfrost droplets on planar ratchets with L_X = 300 μm, but L_Y varying from 120 μm to 250 μm (Supporting Movie 4). Under a smaller L_Y of 120 μm, the Leidenfrost droplet propagates along +X, spanning over the entire surface within a short time. As L_Y is increased to 250 μm, the droplet is rectified into -X, exhibiting a much smaller velocity. However, when L_Y is kept constant at 300 μm instead, Leidenfrost droplets demonstrate decreasing transport velocity in -X direction as L_X is improved from 170 μm to 300 μm (Supporting Movie 5).

We also plotted the variation of the maximum steady velocity as a function of L_Y and L_X, respectively (Figures 3c and 3d). Interestingly, under the same ratchet geometry, there exists a universal L_Y around 230 μm ~ 250 μm, which separate the moving Leidenfrost droplets into

two regimes with opposite directions (Figure 3c). However, if L_X varies instead, Leidenfrost droplets always propagate along the same direction (Figure 3d). In terms of velocity, within the same direction interval, the increase in L_X or L_Y can both lead to the reduction of v_s. Notably, although the variation in Leidenfrost point on different planar ratchets can also affect the maximum steady velocity, the trends present in Figure 3c and 3d are dominant by the structural topography. First, the change of Leidenfrost point only influences the value of droplet velocity other than the transport direction. Second, the Leidenfrost point enhances as L_X and L_Y increases, leading to the larger v_s, which is in opposite to the experimental result. Based on these experimental results, on planar ratchets with the same first-order geometry, the directions of Leidenfrost droplets are solely reliant on the topography of second-order lattice in the direction perpendicular to the central line of ratchet (L_Y), whereas their transport velocities are sensitive to the collective coupling of second-order arrangements in all directions.

To elucidate why the variation in L_Y results in the different directions of Leidenfrost droplets, we conduct theoretical analysis. We first consider the first-order unit. As the vapor flows across the individual ratchet, the resistance acting on the fluid by the ratchet is related to the geometry of the facing body as: $C_D = 2F_D / (\rho_v U^2 A)$, where C_D is the drag coefficient, ρ_v and U are the density and velocity of vapor, respectively, F_D is the drag force and A denotes the frontal area of the object. Based on previous studies, C_D depends on the Reynolds number of escaping vapor (Re) [37, 38], where $\mathrm{Re} = \rho_v U D / \mu_v$, with μ_v being the viscosity of vapor. For a capillary Leidenfrost droplet, the average velocity of vapor flow (U) can be obtained by balancing the evaporation rate of droplet with the mass flow rate of outward Poiseuille flow:

$$\frac{dm}{dt} \sim \frac{k_v (T - T_{sat}) \pi r_c^2}{h_{fg} \delta} \sim \rho_v \pi r_c \delta U \qquad (1)$$

where k_{v} is the thermal conductivity of vapor, h_{fg} denotes the specific latent heat of water

evaporation, $\delta \sim \left[\mu_{\mathrm{v}} k_{\mathrm{v}} \left(T - T_{\mathrm{sat}} \right) r_{\mathrm{c}}^2 / \left(\gamma h_{\mathrm{fg}} \rho_{\mathrm{v}} \right) \right]^{1/4} R_{\mathrm{o}}^{1/4}$, represents the average thickness of vapor

layer [9, 31], $r_{\mathrm{c}} \sim R_{\mathrm{o}}^2 / \kappa^{-1}$, is the radius of the droplet base, $\kappa^{-1} = \left(\gamma / \rho g \right)^{1/2}$, denotes the capillary

length [39], with γ and ρ being the surface tension and density of water at saturation point, g

denoting the gravity acceleration. As a result, our experimental conditions yield a typical Re $\leq$

8. Under this typical Re, we simulated the vapor flow field based on 2D ratchet object using

finite element method (Supporting Text). As evidenced by Figures 4a and 4b, the escaping

vapor displays distinct flow patterns, leading to a smaller drag coefficient in -X direction

($C_{\mathrm{D},-X}$) than that in +X direction ($C_{\mathrm{D},+X}$). Under the large spacing L_Y, the drag coefficient

contrast resulting from the first-order unit can be further reinforced by the ratchet rows cascaded

in X axis, giving rise to a higher rectification ratio of vapor towards -X direction (Figure 4b and

Figure S7). Remarkably, the drag coefficient contrast between these two directions,

$C_{\mathrm{D},-X} / C_{\mathrm{D},+X}$, shows universal dependence on the apex angle of ratchet θ.

The second-order lattice also plays an important role on the rectified vapor flow. First, as

the vapor escapes inside the ratchet arrays, the gaps between adjacent ratchets naturally form

nozzle-shaped channels with wall-to-wall width increasing from $L_Y - D$ at the bottom to L_Y at

the tip (upper panel of Figure 4c). Owing to the larger channel gap, the evaporating vapor is

characterized with a smaller flow resistance and hence a preferential flow in +X direction [40].

Second, based on previous studies [41], the variation in wall-to-wall distance can also modify

the deformation of droplet base. As shown in Figure 4d, we measured the variation of

penetration depth at the center of Leidenfrost droplet on uniform channels with the same base

length of 100 μm (Figure S8). Clearly, under the wall-to-wall distance of 50 μm (corresponding

to L_Y of 150 μm), the increase in wall-to-wall distance can lead to the significant enhancement

in droplet penetration depth (see the dotted-dashed line). The variation in penetration depth

7

becomes less apparent under larger wall-to-wall distance or larger L_Y (see the dashed line). Thus, on planar ratchets with small L_Y, we can expect a gradient in the penetration depth of droplet base owing to the varying wall-to-wall distance between adjacent ratchets. In this regard, a modification of liquid/vapor interface similar to that on conventional millimetric ratchets will occur: it deforms upwards at the base of ratchet ($r_{-X} < 0$) and curves downwards at the tip of ratchet ($r_{+X} > 0$) (see the bottom panel of Figure 4c). As a result, $P_{v,-X} > P_{v,+X}$, which also results in the asymmetric vapor flow along $+X$. Here, P_v represents the pressure inside vapor, which is calculated as [42, 43]: $P_v = P_l - 2\gamma/r$, with P_l being the liquid pressure, r representing the radius of curvature at the liquid/vapor interface. Notably, these two contributions to the rectified vapor flow towards $+X$ direction should be both related to the gradient in wall-to-wall distance of collective channels: $(L_Y - D)/L_Y$.

Under the same first-order geometry, the rectification ratio of evaporation vapor by the individual ratchet is constant regardless of the variation in Y spacing L_Y. However, the rectification of vapor by the collective lattice decreases as L_Y increases. Particularly, as L_Y becomes large enough so that the variation ratio of interactive channel gap is close to 1, the internal coordination between adjacent ratchets can be ignored. As such, the vapor flow is mainly determined by first-order unit, leading to the propagation of droplets towards $-X$ direction. However, when planar ratchets patterned in different rows are close to each other, corresponding to a small L_Y, the second-order asymmetry induces a directional vapor flow and hence a preferential droplet transport in $+X$ direction.

Our model is also substantiated by experimental measurements on planar ratchets with diverse first-order and second-order geometries (Figure S9). As demonstrated in Figure 5, the propagation direction of Leidenfrost droplets on various planar ratchets is dominated by the asymmetries of both first-order unit and second-order lattice. Moreover, the critical second-

order factor L_γ (the dotted line in Figure 5), under which these two-tier asymmetric effects contend equally with each other, decreases as the first-order factor ψ_1 increases, suggesting that the rectified droplet motion along descending slope is preferred on ratchets with larger apex angle. We can envision that synergetic dominances of both individual units and collective arrangements on Leidenfrost droplet dynamics will also occur on other anisotropic planar structures, such as half-cylinders and trapezoid pillars.

In summary, we develop planar ratchets with identical height normal to the surface to enable the rectification of Leidenfrost droplets. Distinct from classic millimetric ratchets where the droplet is manipulated by the geometry of ratchet units alone, droplet dynamics on planar ratchets relies on both the individual features and their collective interplays. We believe that our results can provide new insight into the complicate dynamics of Leidenfrost droplets, and will also impart higher applicability in MEMS-based fluidic devices and drag reduction.

Experimental Section

Sample fabrication: Planar ratchets with various first-order and second-order morphologies were fabricated on silicon wafers through standard photolithography and deep reactive ion etching (DRIE). Here, the thickness of silicon wafer was 420 ± 5 μm. Briefly, after cleaned in the piranha solution (3:1 mixture of H_2SO_4 and H_2O_2 at 120 ℃) for 10 minutes, the silicon wafer was covered with 1 μm of photoresist by standard photolithography. The photoresist acts as the protective mask for the subsequent DRIE process, which includes alternative passivation cycle and etching cycle, with C_4F_8 and SF_6 being the reactants, respectively. After etching the ratchet arrays, the samples were cleaned in the piranha solution for another 10 minutes to completely remove the photoresist mask.

Experimental methods: Planar ratchet samples were taped onto a hot stainless-steel block, whose temperature was controlled by one thermocouple probe and four cartridge heaters (CIR-2036/240V, Omega). Meanwhile, the temperature of the substrate back was real-time monitored by the thermocouple (CO2-K, Omega) patterned at the back of sample. During the experiment, droplets were gently released by the needle from a height equal to the droplet diameter. The droplet transport trajectories on different samples were recorded by high-speed camera (Fastcam SA4, Photron) at a rate of 3,600 frames per second. In addition, the high-speed camera mounted with long-distance microscope (Leica Z16 APO) was adopted to record the deformation at liquid/vapor interface of Leidenfrost droplet.

Image analysis: The velocity of Leidenfrost droplets were calculated by comparing the centroid of droplet between five consecutive frames using ImageJ. And the droplet transport acceleration was obtained by fitting the velocity curve under the velocity of 0 cm/s. Each data point was achieved by taking the average of 10 experimental attempts.

PIV measurement. The polyamide particles with diameter of 5 μm were added to the droplet at a density of ~ 1,200 kg/m^3 as the seeding. During the measurement, the He-Ne laser beam was focused on the central section of the droplet, with a direction in coincidence with the trajectory of moving droplet (Figure S4). After reaching the steady velocity, the flow field inside the droplet was recorded by a high-speed camera at frame rate of 4,000 fps. The captured flow field was further corrected through image mapping to eliminate the optical deformation caused by the droplet, and the detailed information is provided in Supplementary materials.

Supporting Information

Supporting Information is available from the Wiley Online Library or from the author.

References

[1]   D. Quéré, *Annu. Rev. Fluid Mech.* **2013**, 45, 197.

[2]   J. G. Leidenfrost, *De Aquae Communis Nonnullis Qualitatibus Tractatus (Duisburg, 1756).*

[3]   I. U. Vakarelski, N. A. Patankar, J. O. Marston, D. Y. Chan, S. T. Thoroddsen, *Nature* **2012**, 489, 274.

[4]   J. C. Burton, A. L. Sharpe, R. C. A. van der Veen, A. Franco, S. R. Nagel, *Phys. Rev. Lett.* **2012**, 109, 074301.

[5]   H.-m. Kwon, J. C. Bird, K. K. Varanasi, *Appl. Phys. Lett.* **2013**, 103, 201601.

[6]   T. A. Caswell, *Phys. Rev. E* **2014**, 90, 013014.

[7]   M. Shirota, M. A. J. van Limbeek, C. Sun, A. Prosperetti, D. Lohse, *Phys. Rev. Lett.* **2016**, 116, 064501.

[8]   N. Farokhnia, S. M. Sajadi, P. Irajizad, H. Ghasemi, *Langmuir* **2017**, 33, 2541.

[9]   A.-L. Biance, C. Clanet, D. Quéré, *Phys. Fluids* **2003**, 15, 1632.

[10]   J. Li, Y. Hou, Y. Liu, C. Hao, M. Li, M. K. Chaudhury, S. Yao, Z. Wang, *Nat. Phys.* **2016**, 12, 606.

[11]   I. U. Vakarelski, J. O. Marston, D. Y. Chan, S. T. Thoroddsen, *Phys. Rev. Lett.* **2011**, 106, 214501.

[12]   T. Tran, H. J. J. Staat, A. Prosperetti, C. Sun, D. Lohse, *Phys. Rev. Lett.* **2012**, 108, 036101.

[13]   G. Dupeux, M. Le Merrer, C. Clanet, D. Quéré, *Phys. Rev. Lett.* **2011**, 107, 114503.

[14]   A. Hashmi, Y. Xu, B. Coder, P. A. Osborne, J. Spafford, G. E. Michael, G. Yu, J. Xu, *Sci. Rep.* **2012**, 2, 797.

[15]   G. G. Wells, R. Ledesma-Aguilar, G. McHale, K. Sefiane, *Nat. Commun.* **2015**, 6, 6390.

[16]   S. R. Waitukaitis, A. Zuiderwijk, A. Souslov, C. Coulais, M. van Hecke, *Nat. Phys.* **2017**, 13, 1095.

[17]   J. T. Pham, M. Paven, S. Wooh, T. Kajiya, H. J. Butt, D. Vollmer, *Nat. Commun.* **2017**, 8, 905.

[18]   M. K. Chaudhury, A. Chakrabarti, S. Daniel, *Langmuir* **2015**, 31, 9266.

[19]   J. Li, J. Li, J. Sun, S. Feng, Z. Wang, *Adv. Mater.* **2019**, e1806501.

[20]   K. H. Chu, R. Xiao, E. N. Wang, *Nat. Mater.* **2010**, 9, 413.

[21]   J. Li, X. Zhou, J. Li, L. Che, J. Yao, G. McHale, M. K. Chaudhury, Z. Wang, *Sci. Adv.* **2017**, 3, eaao3530.

[22]   J. Li, Q. H. Qin, A. Shah, R. H. Ras, X. Tian, V. Jokinen, *Sci. Adv.* **2016**, 2, e1600148.

[23]   C. Li, N. Li, X. Zhang, Z. Dong, H. Chen, L. Jiang, *Angew. Chem. Int. Ed.* **2016**, 55, 14988.

[24]   J. Liu, H. Guo, B. Zhang, S. Qiao, M. Shao, X. Zhang, X. Q. Feng, Q. Li, Y. Song, L. Jiang, J. Wang, *Angew. Chem. Int. Ed.* **2016**, 55, 4265.

[25]   A. Bouillant, T. Mouterde, P. Bourrianne, A. Lagarde, C. Clanet, D. Quéré, *Nat. Phys.* **2018**, 14, 1188.

[26]   A. Gauthier, C. Diddens, R. Proville, D. Lohse, D. van der Meer, *Proc. Natl. Acad. Sci. U. S. A.* **2019**.

[27]   H. Linke, B. J. Alemán, L. D. Melling, M. J. Taormina, M. J. Francis, C. C. Dow-Hygelund, V. Narayanan, R. P. Taylor, A. Stout, *Phys. Rev. Lett.* **2006**, 96, 154502.

[28]   D. Soto, G. Lagubeau, C. Clanet, D. Quéré, *Phys. Rev. Fluids* **2016**, 1, 013902.

[29]   R. L. Agapov, J. B. Boreyko, D. P. Briggs, B. R. Srijanto, S. T. Retterer, C. P. Collier, N. V. Lavrik, *ACS Nano* **2013**, 8, 860.

[30]   C. Liu, J. Ju, J. Ma, Y. Zheng, L. Jiang, *Adv. Mater.* **2014**, 26, 6086.

[31]   Á. G. Marín, D. Arnaldo del Cerro, G. R. B. E. Römer, B. Pathiraj, A. Huis in 't Veld, D. Lohse, *Phys. Fluids* **2012**, 24, 122001.

[32]   G. Lagubeau, M. Le Merrer, C. Clanet, D. Quéré, *Nat. Phys.* **2011**, 7, 395.

[33]   J. T. Ok, J. Choi, E. Brown, S. Park, *Microelectron. Eng.* **2016**, 158, 130.

[34]   T. R. Cousins, R. E. Goldstein, J. W. Jaworski, A. I. Pesci, *J. Fluid Mech.* **2012**, 696, 215.

[35]   G. Dupeux, M. Le Merrer, G. Lagubeau, C. Clanet, S. Hardt, D. Quéré, *Europhys. Lett.* **2011**, 96, 58001.

[36]   D. Tam, V. von Arnim, G. H. McKinley, A. E. Hosoi, *J. Fluid Mech.* **2009**, 624, 101.

[37]   S. Ganga Prasath, M. Sudharsan, V. Vinodh Kumar, S. V. Diwakar, T. Sundararajan, S. Tiwari, *J. Fluids Struct.* **2014**, 46, 59.

[38]   O. Zeitoun, M. Ali, A. Nuhait, *Int. J. Therm. Sci.* **2011**, 50, 1685.

[39]   Y. Pomeau, M. Le Berre, F. Celestini, T. Frisch, *C.R. Mec.* **2012**, 340, 867.

[40]   X. N. Jiang, Z. Y. Zhou, X. Y. Huang, Y. Li, Y. Yang, C. Y. Liu, *Sens. Actuators, A* **1998**, 70, 81.

[41]   M. Reyssat, J. M. Yeomans, D. Quéré, *Europhys. Lett.* **2008**, 81, 26006.

[42]   M. J. Fuerstman, A. Lai, M. E. Thurlow, S. S. Shevkoplyas, H. A. Stone, G. M. Whitesides, *Lab on a chip* **2007**, 7, 1479.

[43]   H. Kim, B. Truong, J. Buongiorno, L. W. Hu, *Appl. Phys. Lett.* **2011**, 98, 083121.
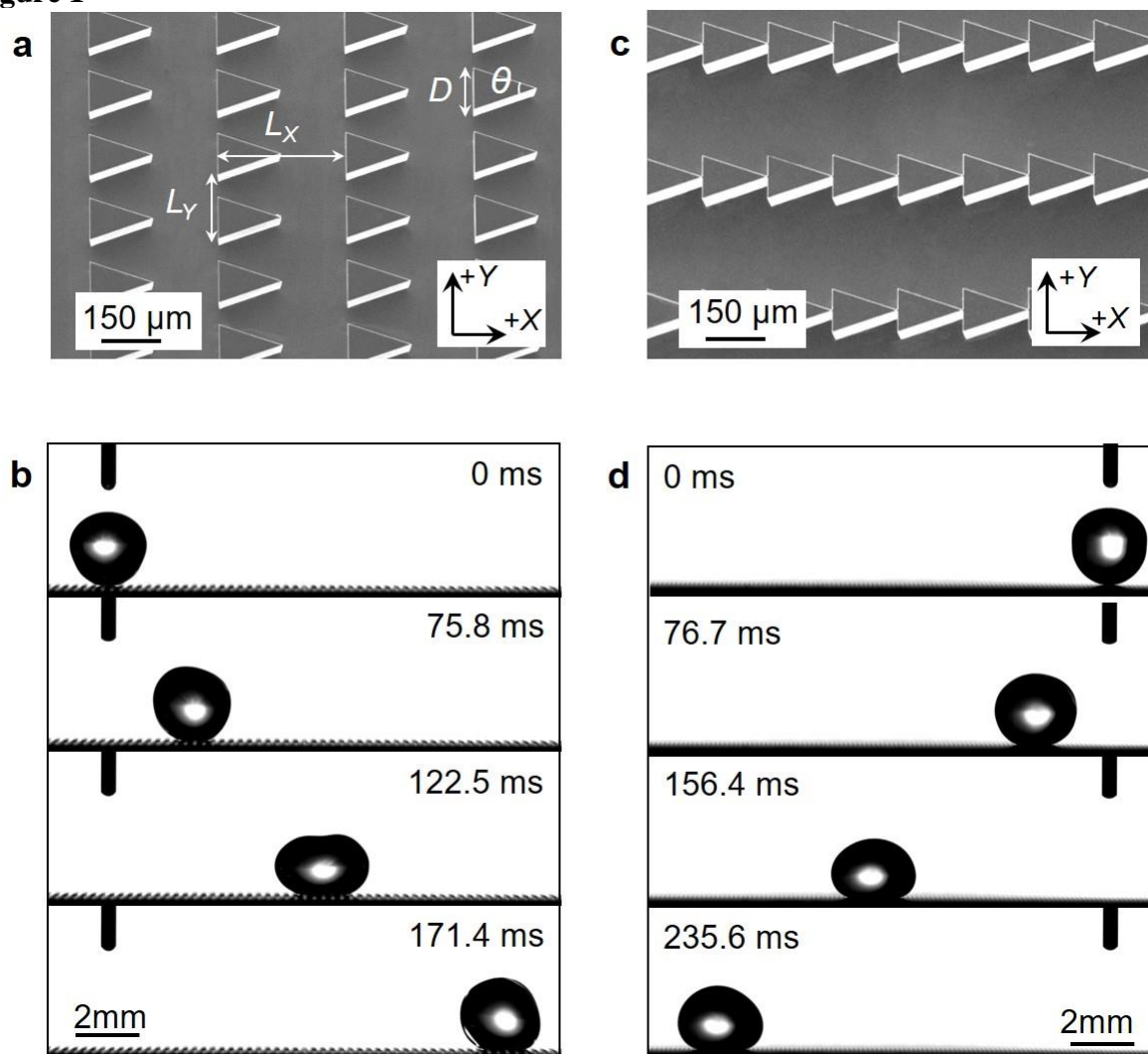
Figure 1

Figure 1. Leidenfrost droplets rectified by planar ratchets. (a) Scanning Electron Microscopic (SEM) image of planar ratchets with spacings in X (L_X) and Y (L_Y) directions set at 300 μm and 150 μm, respectively. (b) Selected snapshots showing the directional transport of Leidenfrost droplet ($T_L = 300 \pm 6.0$ °C) on the planar ratchets in $+X$ direction. (c) SEM image of planar ratchets with reverse spacings: $L_X = 150$ μm and $L_Y = 300$ μm. (d) Selected snapshots of the Leidenfrost droplet ($T_L = 305 \pm 6.1$ °C) on surface with reverse spacings, displaying the opposite $-X$ direction.

Figure 2
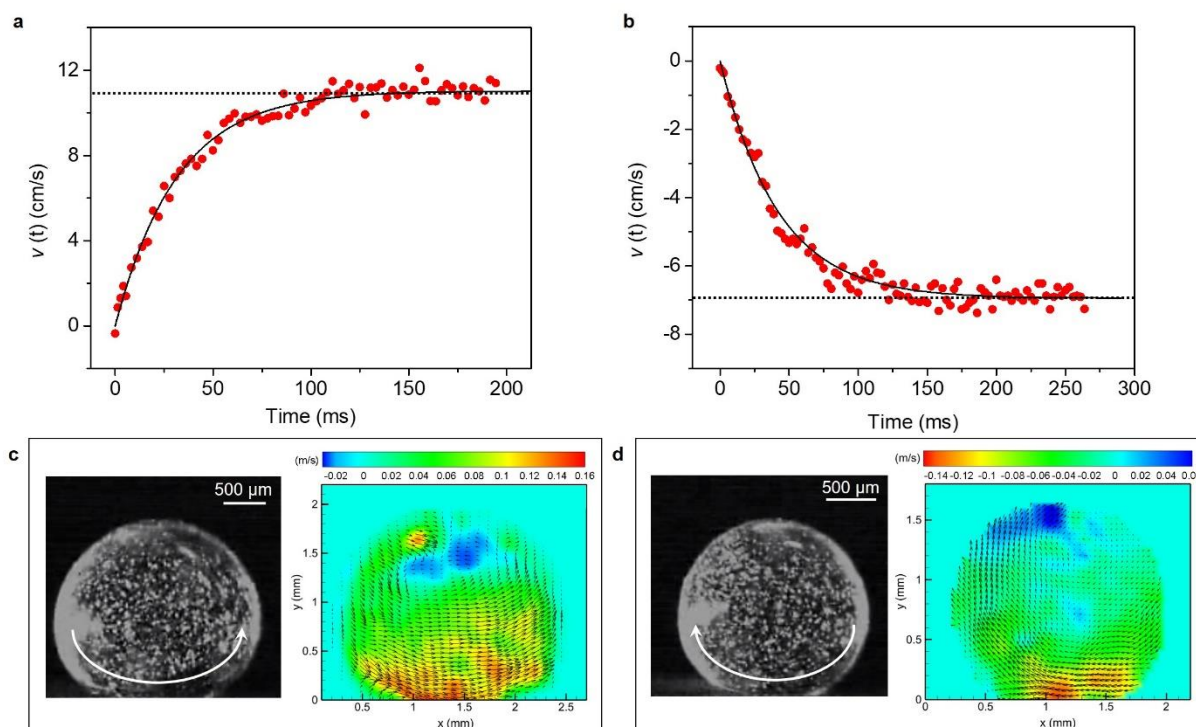
Figure 2. Characterization of droplet dynamics on planar ratchets. (a) Time evolution of droplet transport velocity at Leidenfrost state on planar ratchets with $L_X = 300$ μm and $L_Y = 150$ μm. (b) The variation of Leidenfrost droplet velocity on planar ratchets with switched spacings ($L_X = 150$ μm and $L_Y = 300$ μm) as a function of time. The error bars denote the standard deviations of the measurements. (c, d) PIV measurements revealing the inner velocity fields of Leidenfrost droplets on planar ratchets with different second-order arrangements: (c) $L_X = 300$ μm, $L_Y = 150$ μm; (d) $L_X = 150$ μm, $L_Y = 300$ μm. Note that all the data was achieved at Leidenfrost points of planar ratchets.
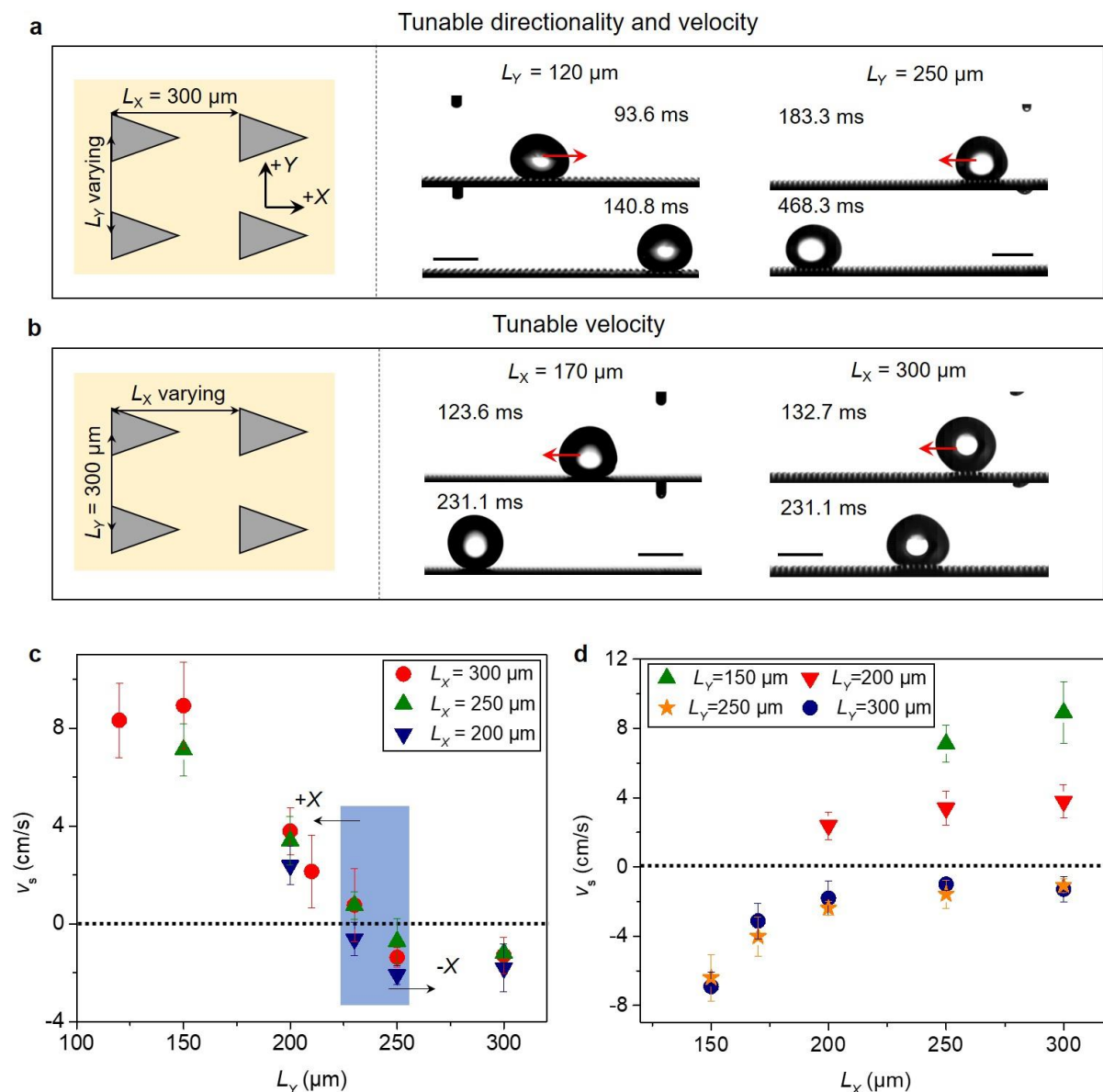
Figure 3

Figure 3. Leidenfrost droplet dynamics mediated by second-order asymmetry. (a) Selected snapshots showing the movement of Leidenfrost droplets on planar ratchets with $L_Y = 120$ μm and 250 μm, respectively. Here, $L_X = 300$ μm. The scale bars denote 2 mm. (b) Selected snapshots presenting the droplet transport dynamics on surfaces with L_X varying from 170 μm to 300 μm, respectively. Here, $L_Y = 300$ μm. The scale bars are 2 mm. (c) The variation of v_s as a function of L_Y. (d) The variation of v_s as a function of L_X. All the error bars represent the standard deviations of the measurements. Note that the apex angle θ and base length D of first order unit are kept constant at 37° and 100 μm, respectively.
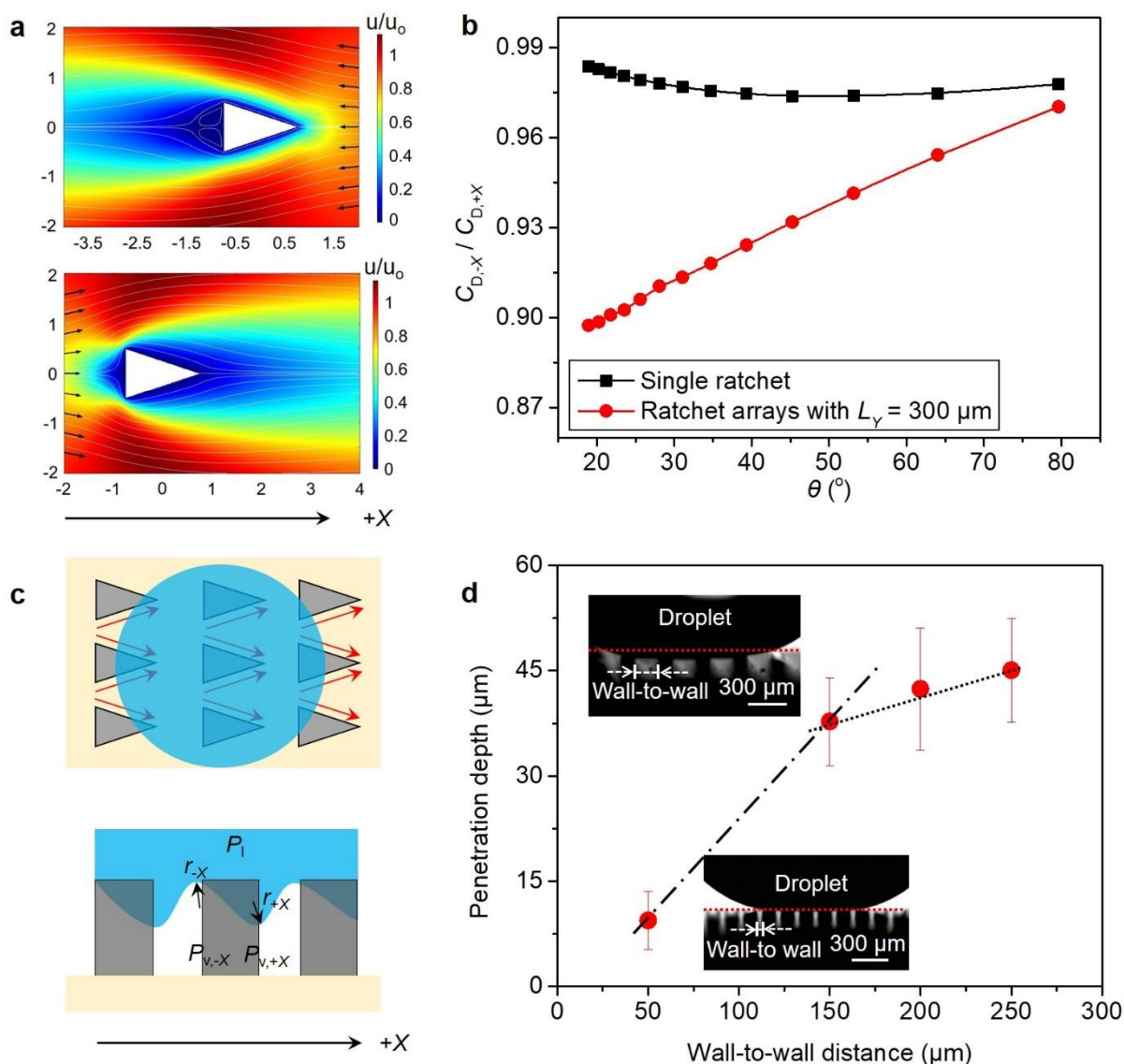
Figure 4

Figure 4. The dependence of droplet moving directions on the first-order and second-order asymmetries. (a) Flow fields of vapor across the first-order unit in different directions under Re = 8. (b) Simulated drag coefficient ratio at Re = 8 as a function of the apex angle θ of first-order unit. (c) Schematic images showing the preferential vapor flow rectified by second-order lattice. The upper panel reveals the asymmetric vapor flow towards the larger opening of nozzle-shaped channels, which are formed between adjacent ratchets. The lower panel demonstrates the deformation of liquid/vapor interface caused by the varying channel gap. (d) The variation of droplet penetration depth as a function of wall-to-wall distance between channels. The results were measured on uniform channels with base length of 100 μm. The

inserts show corresponding optical images revealing the deformation of liquid/vapor interface on channels with mutual gaps of 50 μm and 150 μm, respectively. And the red dotted line in the inserts represents the top of ratchets. The error bars denote the standard deviations of the measurements.
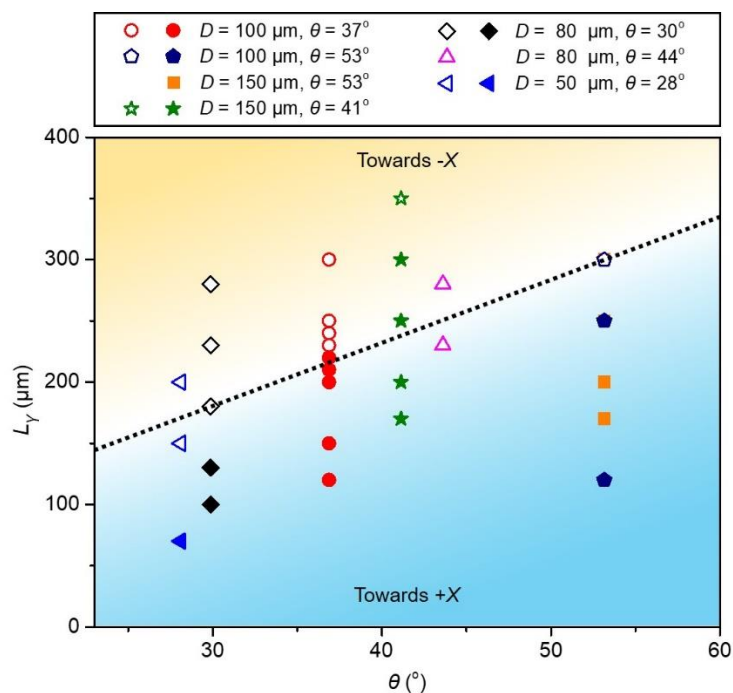

Figure 5. Experimental phase diagram revealing the droplet transport directionality on planar ratchets with concurrently varying first-order and second-order arrangements. Here, filled and open symbols represent the droplet rectification towards +*X* and -*X*, respectively. The dotted line denotes the experimental condition in which the first-order effect is matched with second-order coordination.

The table of contents:

Two-dimensional planar ratchets are developed to enable the rectification of Leidenfrost droplets. Distinct from classic millimetric ratchets where Leidenfrost droplet moves along the asymmetric ratchet, droplet on planar ratchets relies on both the individual features and their collective arrangements. What results in is the varying droplet mobility ranging from 10 cm/s along the descending slope to -7 cm/s against the descending slope.

Keyword: rectification, individual effect, collective coordination, Leidenfrost droplet, fluidic devices
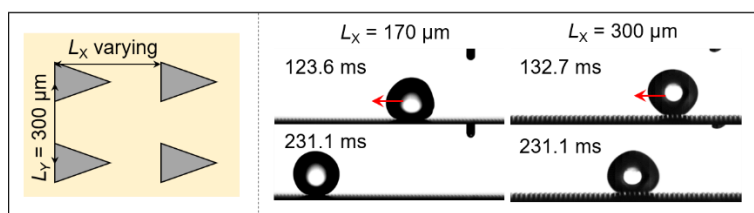
J. Li, X. Zhou, Y. Zhang, C. Hao, F. Zhao, M. Li, H. Tang, W. Ye, and Z. Wang*

Rectification of mobile Leidenfrost droplets by planar ratchets
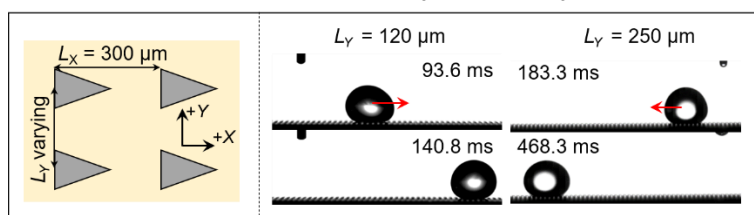
Supporting Information

Rectification of mobile Leidenfrost droplets by planar ratchets

Jing Li, Xiaofeng Zhou, Yujie Zhang, Chonglei Hao, Fuwang Zhao, Minfei Li, Hui Tang, Wenjing Ye, and Zuankai Wang*

Captions of Supporting Movies

Supporting Movie 1. Rectification of Leidenfrost droplet on planar ratchets with second-order spacings, L_X and L_Y, set at 300 μm and 150 μm, respectively. After gentle deposition, the Leidenfrost droplet demonstrates a long-range propagation along the descending slope of ratchet (or $+X$).

Supporting Movie 2. Rectification of Leidenfrost droplet on planar ratchets with reverse spacings ($L_X = 150$ μm and $L_Y = 300$ μm). Upon reaching the Leidenfrost point (305 ± 6.1 °C), the droplet propagates in $-X$ direction, which is opposite to that manifested on two-tier surface with $L_X = 300$ μm and $L_Y = 150$ μm.

Supporting Movie 3. Leidenfrost droplets gently placed on control surfaces with second-order asymmetry alone. Remarkably, Leidenfrost droplets show no preferential movement no matter how the feature spacings in X and Y axes, *i.e.* L_X and L_Y, vary.

Supporting Movie 4. Rectified droplet transport on planar ratchets with L_X fixed at 300 μm and L_Y increasing. Under the identical L_X, the variation in L_Y leads to the tunability in both transport velocity and directionality of moving Leidenfrost droplets.

Supporting Movie 5. Rectified droplet transport on planar ratchets with L_Y fixed at 300 μm but L_X increasing. Under the same L_Y, Leidenfrost droplets demonstrate decreasing velocity in the same direction as L_X increases.

Supporting Information text

S1. Flow field inside Leidenfrost droplet

The flow fields inside Leidenfrost droplets were compared using Particle Image Velocimetry (Figure S4). During the PIV measurements, the spherical liquid droplet acts like magnifying lens, which distorts the flow filed of its central cross-section. To eliminate such an optical deformation, the measured flow field was corrected by image mapping using Tam *et al.*'s method [36]. Specifically, assuming point M (p, l) on the middle cross-section, its optical image after reflection becomes M' (p', l'), where p and l represent the distances from the particle to the central cross-section plane and the optical axis, respectively, while p' and l' are the distances from the optical image of particle to the central cross-section plane and the optical axis, respectively. Based on the Snell-Descartes law, the optical image of particle M' can be related to its real position M ($p = 0$) as:

$$p^{'} = g(l) = -\frac{n_{\text{water}}}{n_{\text{air}}} l \sin\left[\arcsin l - \arcsin\left(\frac{n_{\text{water}}}{n_{\text{air}}} l \right) \right] \tag{S1}$$

$$r^{'} = f(l) = \frac{n_{\text{water}}}{n_{\text{air}}} l \cos\left[\arcsin l - \arcsin\left(\frac{n_{\text{water}}}{n_{\text{air}}} l \right) \right] \tag{S2}$$

with n_{water} and n_{air} being the refractive index of water at 100 $^{\text{o}}$C and air, respectively.

S2. COMSOL simulation of drag coefficients for vapor to flow in different directions

Due to the small Reynolds number and thus the low Mach number, we assumed that the gas flow was incompressible and laminar. Thus, the governing equation can be expressed as:

$$\frac{\partial u_i}{\partial t} + \frac{\partial}{\partial x_j} u_i u_j = -\frac{\partial P}{\partial x_i} + \frac{1}{\text{Re}} \frac{\partial}{\partial x_j} \frac{\partial}{\partial x_j} u_i ; \frac{\partial u_i}{\partial x_i} = 0 \tag{S4}$$

22

with x_i being the Cartesian coordinates, and u_i denoting the velocity components. Note that all variables were non-dimensionalized by the triangle base D or the free-stream velocity u_∞. Under steady state at low Reynolds number, $\partial u_i / \partial t = 0$.

For the case of single unit, two-dimensional ratchet objects with constant D but varying ψ_1 are confined in a large rectangular box with length and width set at $50D$ and $40D$, respectively. The employed boundary conditions for the simulation are specified as below:

Inlet boundary: $u_x = u_\infty$, $u_y = 0$; Outlet boundary: $\partial u_x / \partial x = 0$, $\partial u_y / \partial x = 0$ and $P = P_o$;

Lateral boundaries: $u_y = 0$, $\partial u_x / \partial y = 0$.

To explore how the rectification of vapor rendered by individual ratchet can be reinforced by the arrangement of second-order lattice, we also simulated and compared the drag coefficient of ratchet patterned at the center of ratchet arrays under the large spacing L_Y of 300 μm. Specifically, periodical ratchet rows consist of seven objects, with the overall length of ratchet rows comparable to the base diameter of Leidenfrost droplets. Meanwhile, the length and width of computational domain are set at $3D$ and $27D$, respectively. The corresponding boundary conditions are listed as below:

Inlet boundary: $u_x = u_\infty$, $u_y = 0$; Outlet boundary: $\partial u_x / \partial x = 0$, $\partial u_y / \partial x = 0$ and $P = P_o$;

Lateral boundaries: Periodic boundary conditions

Finally, all the equations were solved by finite element method using COMSOL software.

As revealed by our simulation result in Figures 4a and 4b, the evaporating vapor encounters smaller drag coefficient in -X owing to the asymmetric geometry of individual ratchet. Moreover, the drag coefficient contrast in different directions can be further reinforced by the ratchet rows cascaded along X axis (Figure S7), leading to a preferential vapor flow and thus the droplet transport along -X.
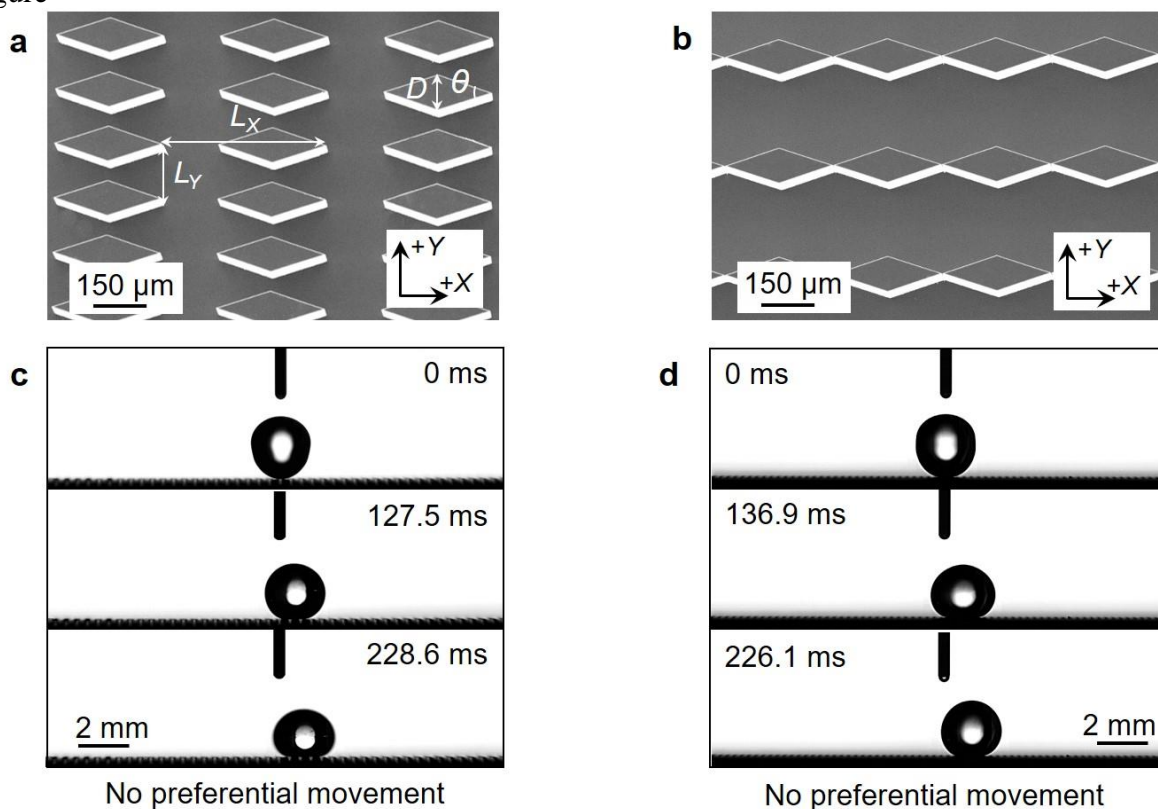
Figure

Figure S1. Leidenfrost droplets on control surface with second-order asymmetry alone. (a) SEM image of control surface featuring with symmetric rhombus-shaped posts patterned in rectangular lattice. These individual rhombus-shaped posts, serving as the first-order units, are symmetric in both lateral (or along X axis) and perpendicular (or along Y axis) directions, with the length of the rhombic base D, the apex angle θ, and the post height h fixed at 100 µm, 37°, and 100 µm, respectively. In contrast, the length and width of rectangular lattice (*i.e.* L_X and L_Y) change, giving rise to the second-order asymmetry. (b) SEM image of control surface with L_X and L_Y being 300 µm and 300 µm, respectively ($T_L = 250 \pm 5.0$ °C). (c) Selected snapshots showing the Leidenfrost droplet gently deposited on control surface with $L_X = 450$ µm and $L_Y = 150$ µm, where no preferential movement was observed. (d) Selected snapshots showing the Leidenfrost droplet on control surface with $L_X = 300$ µm and $L_Y = 300$ µm, demonstrating no directional motion ($T_L = 220 \pm 4.4$ °C).
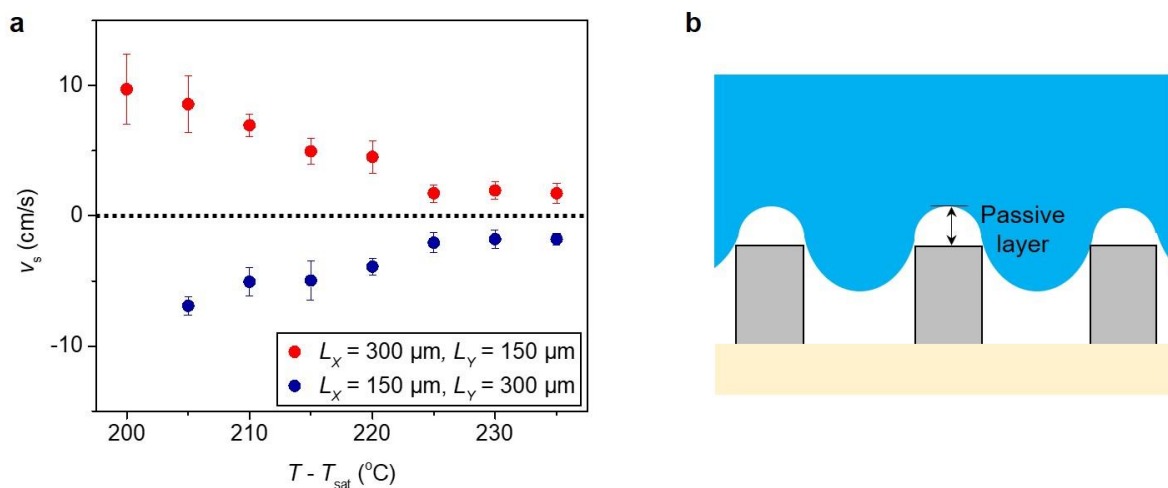
Figure S2. The effect of superheat on the transport of Leidenfrost droplets. (a) The variation of droplet steady velocity on planar ratchets as a function of superheat (T - T_{sat}). On both surfaces, the stable velocities decrease as the superheat increases. The error bars correspond to the standard deviations of the measurements. (b) Schematic image showing the geometry of the evaporating vapor layer underneath the Leidenfrost droplet. Specifically, as the superheat increases, the vapor layer inflating above the planar ratchets (or the passive layer) becomes thicker, which screens the effects of asymmetric structures and impairs the directional motion of Leidenfrost droplets.
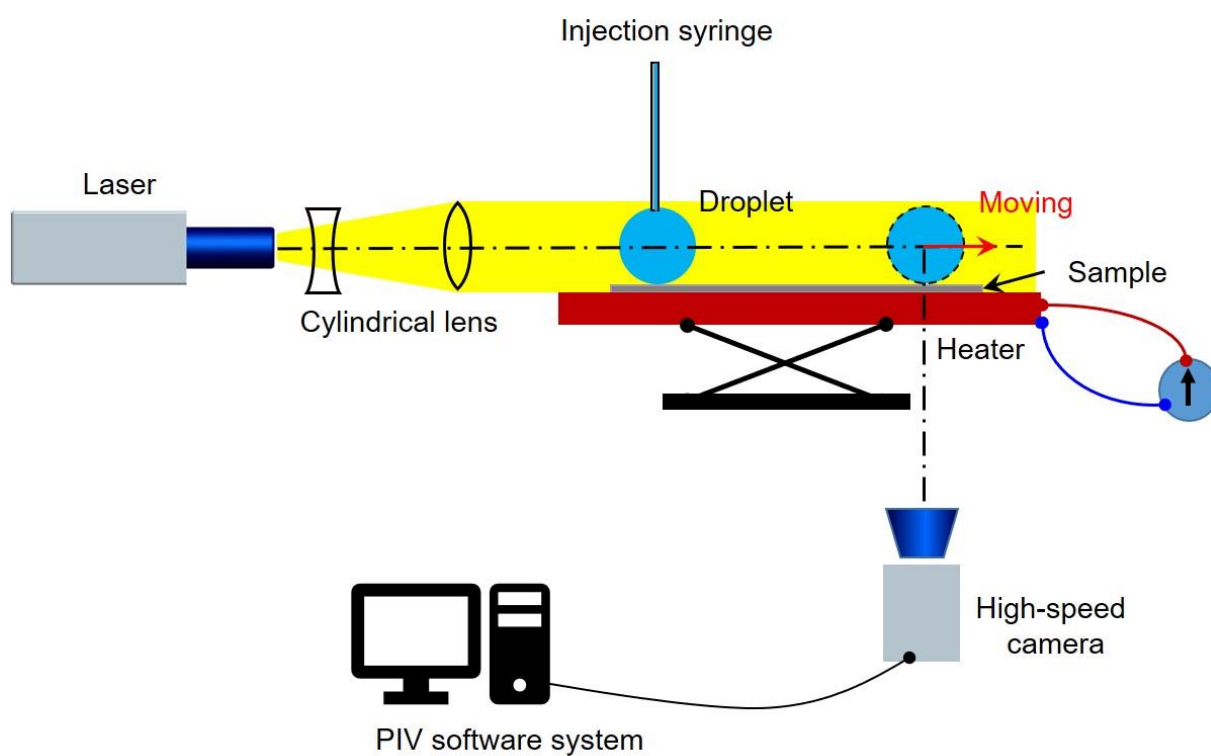
Figure S3. Schematic image illustrating the experimental setup for Particle Image Velocimetry (PIV). During the measurement, the laser was adjusted to be coincident with the transport trajectory of moving Leidenfrost droplet.
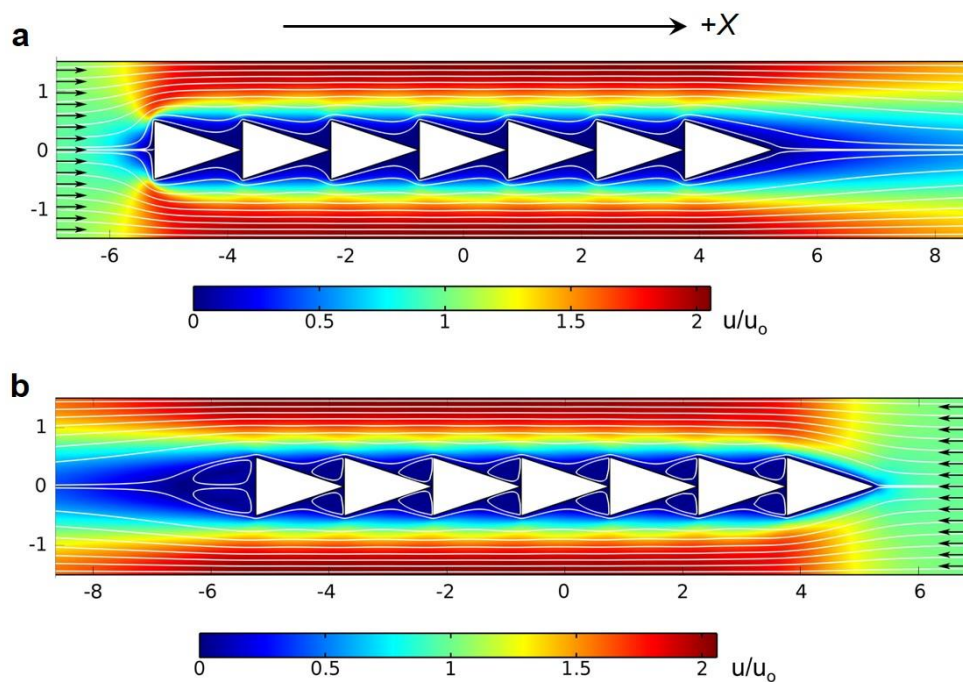
Figure S4. Streamlines as vapor flows across periodical ratchet arrays with spacing L_Y of 300 μm (Re = 8). (a) Vapor flows towards -X. (b) Vapor flows towards +X. Clearly, owing to the asymmetric geometry of planar ratchets, the vapor demonstrates distinct flow fields in these directions.
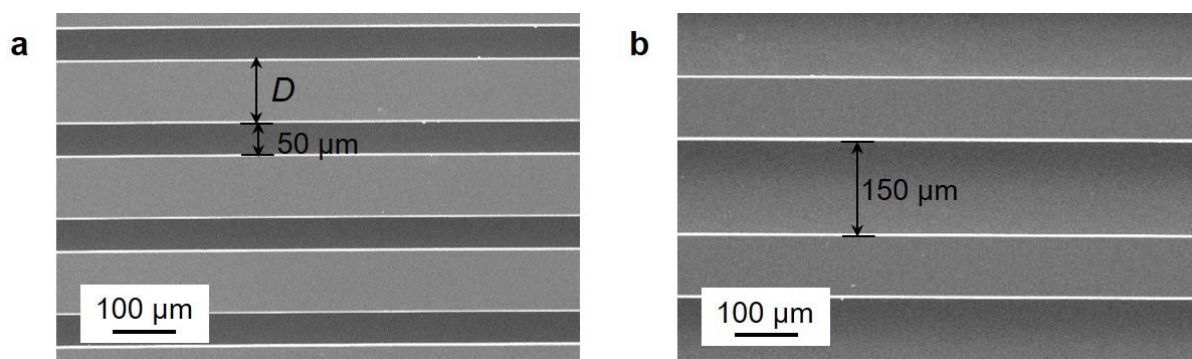
Figure S5. SEM images showing the channels with uniform wall-to-wall distance. (a) Channels with small wall-to-wall distance of 50 μm. (b) Channels with large wall-to-wall distance of 150 μm. The base length of the channel *D* is set at 100 μm.
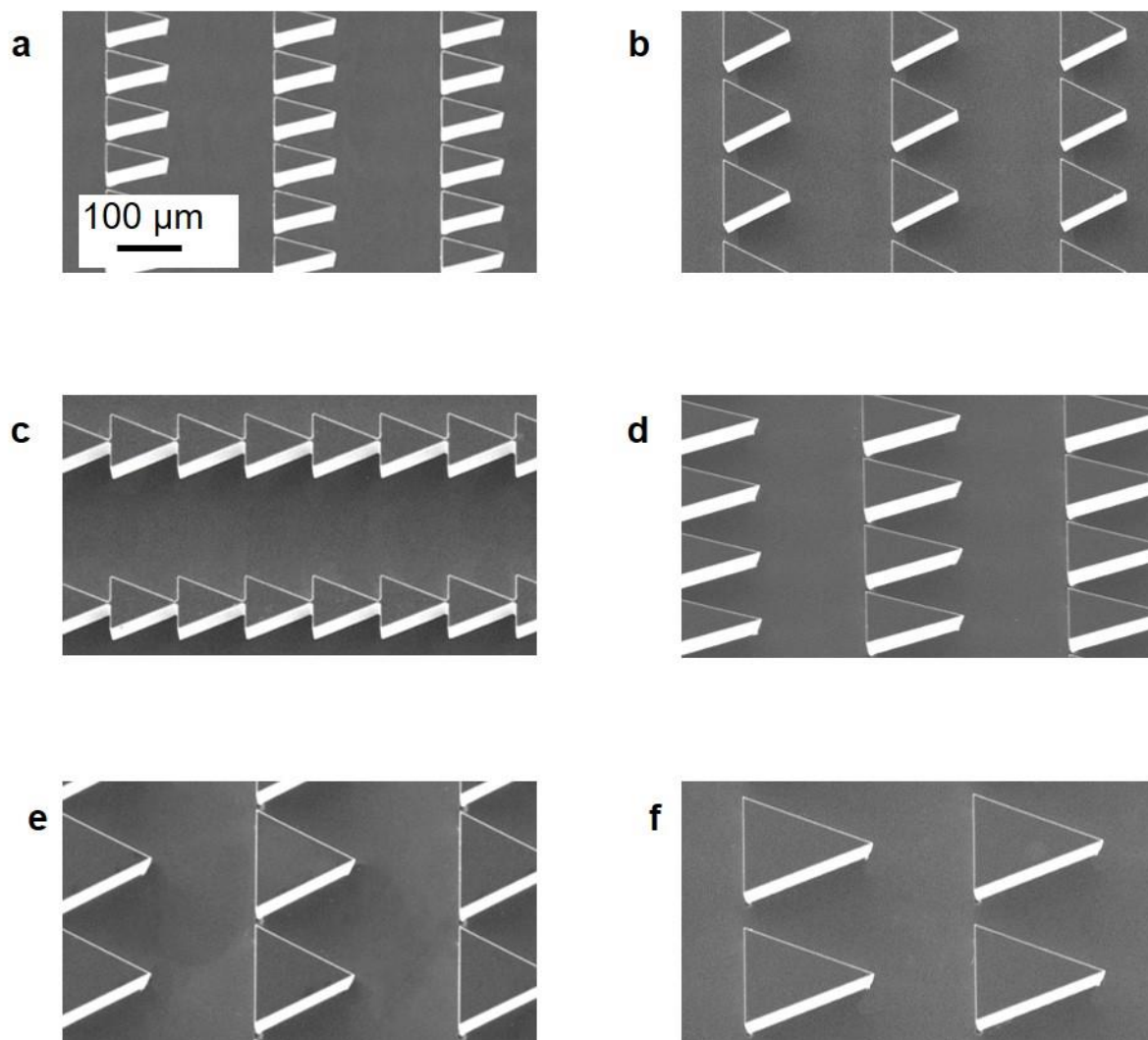
Figure S6. SEM images showing the planar ratchets with various first-order geometry. (a) $D = 50$ μm, $\theta = 28°$. (b) $D = 100$ μm, $\theta = 53°$. (c) $D = 80$ μm, $\theta = 44°$. (d) $D = 80$ μm, $\theta = 30°$. (e) $D = 150$ μm, $\theta = 53°$. (f) $D = 150$ μm, $\theta = 41°$.

Table S1. The first-order and second-order parameters as well as their corresponding

Leidenfrost points of various planar ratchets with L_X fixed but L_Y varied.

Second-order spacing (μm)		Frist-order structure (μm)		T_L (ºC)	Second-order spacing (μm)		Frist-order structure (μm)		T_L (ºC)
L_X	L_Y	D	θ		L_X	L_Y	D	θ	
200	200			280 ± 5.6	250	300	100	37º	335 ± 6.7
200	230	100	37º	285 ± 5.7	300	120			290 ± 5.8
200	250			290 ± 5.8	300	150			300 ± 6.0
200	300			310 ± 6.2	300	200			325 ± 6.5
250	150			290 ± 5.8	300	210	100	37º	330 ± 6.6
250	200	100	37º	305 ± 6.1	300	230			335 ± 6.7
250	230			310 ± 6.2	300	250			345 ± 6.9
250	250			320 ± 6.4	300	300			350 ± 7.0

Table S2. The first-order and second-order parameters as well as their corresponding Leidenfrost points of various planar ratchets with L_Y fixed but L_X varied.

Second-order spacing (μm)		First-order structure (μm)		T_L (°C)	Second-order spacing (μm)		First-order structure (μm)		T_L (°C)
L_Y	L_X	T_L	θ		L_Y	L_X	D	θ	
150	250	100	37°	290 ± 5.8	250	250	100	37°	320 ± 6.4
150	300			300 ± 6.0	250	300			345 ± 6.9
200	200			280 ± 5.6	300	150			305 ± 6.1
200	250	100	37°	305 ± 6.1	300	170			305 ± 6.1
200	300			325 ± 6.5	300	200	100	37°	310 ± 6.2
250	150			285 ± 5.7	300	250			335 ± 6.7
250	170	100	37°	300 ± 6.0	300	300			350 ± 7.0
250	200			290 ± 5.8					